

# Construction of Smooth Flux Surfaces via Multiple Field-Line Tracings

Seikichi MATSUOKA<sup>1,2)</sup>

<sup>1)</sup> National Institute for Fusion Science, Toki 509-5292, Japan

<sup>2)</sup> The Graduate University for Advanced Studies, SOKENDAI, Toki 509-5292, Japan

(Received 12 June 2021 / Accepted 2 September 2021)

In this study, a new numerical method for constructing flux surfaces for three-dimensional (3D) toroidal magnetic fields is proposed. In the method, multiple field lines starting from all grid points in the computational domain are simultaneously followed to obtain the field-line average. The field-line average obtained for the entire domain is used to label flux surfaces as the radial coordinate based on a reasonable assumption that the field-line average approximates the flux surface average when continuous nested surfaces exist. It is demonstrated that a severe numerical discontinuity in the constructed surfaces, which is often observed near a low-order rational surface in a conventional method based on the Poincaré map, can be avoided using the proposed method, enabling the construction of smooth flux surfaces.

© 2021 The Japan Society of Plasma Science and Nuclear Fusion Research

Keywords: magnetic coordinate, flux surface, stellarator, heliotron, field-line tracing

DOI: 10.1585/pfr.16.1403097

## 1. Introduction

The construction of magnetic coordinates is a fundamental requirement to study magnetically confined plasmas. It is done by finding a transformation between the magnetic coordinates  $(\rho, \theta, \zeta)$  and ordinary spatial coordinates e.g., cylindrical coordinates  $(R, \phi, Z)$ , where  $\rho$  denotes the label of the flux surfaces, and  $\theta$  and  $\zeta$  are the poloidal and toroidal angle-like variables, respectively. To this end, a family of continuous nested flux surfaces spanning from the magnetic axis to the last closed flux surface (LCFS) should be constructed for a given magnetic field in a torus plasma. In axisymmetric tokamaks, the magnetic field is two-dimensional, and nested surfaces always exist owing to the symmetry. That means, there are no difficulties in the construction of the magnetic coordinates. In contrast, in three-dimensional (3D) devices, the existence of the nested surfaces is not guaranteed owing to the absence of symmetry. Because the existence of surfaces in a certain region in a 3D device cannot be known *a priori*, the numerical construction of flux surfaces with sufficient accuracy is difficult even when the nested surfaces exist.

Thus far, several methods have been proposed to identify positions of flux surfaces and to construct magnetic coordinates for 3D magnetic field configurations [1–8]. Although there are many differences among the methods, they commonly rely on long-field line tracing to obtain their coordinate values on a flux surface. Because a field line lies on a flux surface, successive points obtained by field-line tracing belong to a surface specified by the initial point  $(R, \phi, Z) = (R_{\text{ini}}, \phi_{\text{ini}}, Z_{\text{ini}})$ . That is, each field

line has a one-to-one relationship with a surface. Then, the transformation between  $(\rho, \theta, \zeta)$  and  $(R, \phi, Z)$  on the surface can be constructed by either Fourier transformation along the field line [1–4, 7] or directly interpolating successive points [8]. The procedure is repeated, while changing the initial point  $(R_{\text{ini}}, \phi_{\text{ini}}, Z_{\text{ini}})$ , or the surface, which determines the global transformation defined from the axis to LCFS.

Although the methods based on long-field line tracing work well for many regions of interest with good nested surfaces, as we shall see later, the derivative  $(\partial/\partial\rho, \partial/\partial\theta, \text{and } \partial/\partial\zeta)$  of the transformation often suffers from numerical discontinuity near a low-order rational surface, causing the discontinuity in other metric coefficients and the Jacobian. The cause of the discontinuity is still unclear and has not been fully addressed in this study as it could be closely related to more difficult questions of nonlinear resonance and the formation of islands/chaos near the rational surface. However, from the viewpoint of subsequent calculations such as instability analyses and/or transport simulations, it is necessary to construct globally smooth coordinates without any discontinuity in computational domain since they are usually performed in the magnetic coordinates  $(\rho, \theta, \zeta)$ .

To overcome the discontinuity, we propose a novel numerical method to construct smooth flux surfaces, or radial coordinate  $\rho$ , for an arbitrary magnetic field in this study. The method is called dense mapping. In the method, multiple field lines starting from all grid points in the computational domain are simultaneously followed to compute the average along each field line. Then, the field-line average obtained over the entire domain is used to label flux sur-

author's e-mail: matsuoka.seikichi@nifs.ac.jp

faces as the radial coordinate  $\rho$  based on a reasonable assumption that the field-line average can be regarded as an approximation of the flux surface average in 3D magnetic fields with continuous nested surfaces. It is demonstrated that the above discontinuity can be successfully avoided because of the smoothing effect on  $\rho$  in the method.

The rest of this paper is organized as follows. A new numerical method to construct smooth flux surfaces using multiple field-line tracings, dense mapping, is described in Sec. 2. A brief description of a conventional method based on long field-line tracing and the Poincaré map is also presented in this section. In Sec. 3, two methods are applied to a model stellarator magnetic field. The constructed magnetic surfaces and relevant geometrical quantities are examined by comparing the new method with the conventional method. Finally, Sec. 4 presents the summary.

## 2. Numerical Construction of Flux Surfaces

In this section, two numerical methods to construct flux surfaces are described. First, a method based on the Poincaré map, where a single field-line tracing is performed to construct a transformation on a surface, is briefly reviewed in Sec. 2.1. Thereafter, in Sec. 2.2, dense mapping method based on multiple field-line tracings is presented.

### 2.1 Construction of surfaces based on the Poincaré map

The starting point is the equations of a magnetic field line in the cylindrical coordinates  $(R, \phi, Z)$ :

$$\frac{dl}{B} = \frac{dR}{B^R} = \frac{d\phi}{B^\phi} = \frac{dZ}{B^Z}, \quad (1)$$

where  $B^u = \mathbf{B} \cdot \nabla u$  ( $u = R, \phi, Z$ ) is the contravariant component of  $\mathbf{B}$ , and  $dl$  denotes the arc length along the field line. Assuming that  $B^\phi$  is non-vanishing, which is true for toroidal devices such as tokamaks and stellarators/heliotrons, we obtain the following set of equations from Eq. (1):

$$\frac{dR}{d\phi} = \frac{B^R}{B^\phi}, \quad (2)$$

$$\frac{dZ}{d\phi} = \frac{B^Z}{B^\phi}. \quad (3)$$

A magnetic field line is followed using Eqs. (2) and (3). Consequently, one can obtain successive puncture points of  $(R, Z)$  at each  $\phi$  step, yielding the Poincaré map on each  $\phi$ -fixed plane. The successive points belong to a flux surface specified by the initial value of  $(R, Z)$  at  $\phi = 0$ . The surface is denoted by  $\rho$ , which is defined later in this subsection. It should be noted that successive points on each  $\phi$ -fixed plane become dense and form a closed line when the rotational transform  $\tau$  of the surface is irrational. If the surface is found to be a low-order rational surface, then the

initial point must be displaced by a small amount to discard the surface since a closed line cannot be constructed within an acceptable accuracy on the surface.

We now have successive points of  $R$  and  $Z$  on  $\phi$ -fixed planes belonging to a  $\rho$  surface. Therefore, we can construct the local transformation between  $(R, \phi, Z)$  and  $(\rho, \theta, \zeta)$  on the surface. For this purpose, it is convenient to introduce other coordinates  $(r, \vartheta, \zeta)$ , where  $r \equiv \sqrt{(R - R_{\text{ax}})^2 + (Z - Z_{\text{ax}})^2}$  is the radius measured from the magnetic axis  $(R_{\text{ax}}, Z_{\text{ax}})$  on each  $\phi$  plane,  $\vartheta \equiv \tan^{-1} [(R - R_{\text{ax}}) / (Z - Z_{\text{ax}})]$  is the geometrical poloidal angle, and  $\zeta \equiv -\phi$  is the toroidal angle. Note that the position of  $(R_{\text{ax}}, Z_{\text{ax}})$  varies depending on  $\phi$  and must be identified in advance to obtain  $r$  and  $\vartheta$ . Using this definition, the successive points of  $R$  and  $Z$  for each  $\rho$  and  $\phi$  are combined into  $r$ , which is then regarded as a function of only  $\theta$  by choosing the poloidal angle of the magnetic coordinates as  $\theta = \vartheta$ , that is,  $r = r(\theta; \rho, \zeta)$  with both  $\rho$  and  $\zeta$  being fixed. Interpolating  $r$  in the  $\theta$  direction on every  $\zeta = -\phi$  plane gives the local transformation between  $(r, \vartheta, \zeta)$  and  $(\rho, \theta, \zeta)$  on each  $\rho$  surface.

Next, the procedure is repeated, while changing the initial point, or surface  $\rho$ . The coordinate  $\rho$  is chosen such that  $\rho$  is monotonically increasing with  $\rho = 0$  at the magnetic axis and  $\rho = 1$  at the LCFS. Choosing  $\rho = r^*/a_0 \equiv \rho_{\text{PM}}$  meets the requirement, where  $r^* = r(\vartheta = 0, \zeta = 0)$  is the radius measured along the line segment at  $(\vartheta, \zeta) = (0, 0)$  (the line segment from the axis to the LCFS along  $Z = 0$  on the  $\phi = 0$  plane), and  $a_0$  denotes  $r^*$  at the LCFS along the line segment, which must be identified before the mapping. Finally, connecting  $r$  in the  $\rho$  direction by interpolation yields the global transformation between  $(r, \vartheta, \zeta)$  and magnetic coordinates  $(\rho_{\text{PM}}, \theta, \zeta)$ . Hereafter, we refer to the method based on the Poincaré map as simple mapping, and Fig. 1 (a) depicts a schematic view of the method. In Fig. 1 (a), the  $i$ -th surface denotes the surface determined by field-line tracing starting from the initial point of  $(r, \vartheta, \zeta) = (r_i = i\Delta r, 0, 0)$  ( $i = 1, 2, 3, \dots$ ), where  $\Delta r = a_0/N_r$ , and  $N_r$  is the number of radial grids. Simple mapping is similar to the method proposed by Predebon *et al.* [8], where they used the poloidal angle of straight field line coordinates instead of the geometrical angle used here with the help of  $\tau$  evaluated using a more sophisticated technique.

### 2.2 Dense mapping based on multiple field-line tracings

Our approach is an extension of Todoroki's method [9], which computed the rotational transform  $\tau$  with high accuracy for any magnetic field line. From Ref. [9], the geometrical poloidal angle  $\vartheta$  along the field line is related to the toroidal angle  $\zeta = -\phi$  as follows:

$$\frac{d\vartheta}{d\zeta} = \tau + \sum_{m,n} i c_{mn} \omega_{mn} \exp(i\omega_{mn}\zeta), \quad (4)$$

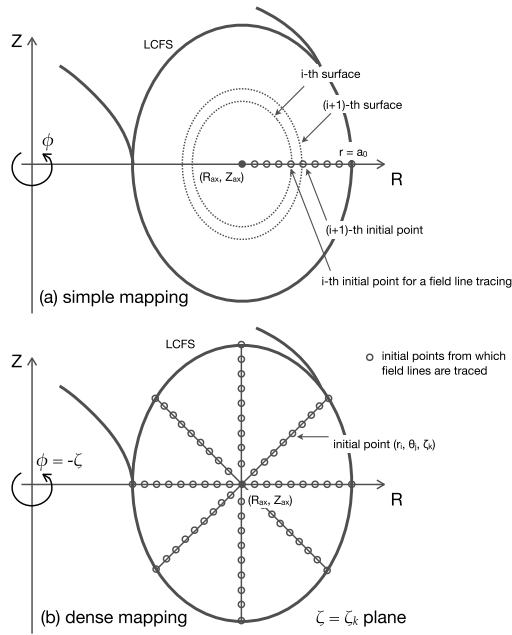


Fig. 1 Schematic views of (a) simple mapping and (b) dense mapping to construct flux surfaces. In dense mapping (b), only the  $k = 1$  ( $\zeta = 0$ ) plane is illustrated for simplicity.

where  $c_{mn}$  represents the Fourier components of  $\vartheta$ ,  $\omega_{mn} = m - n$ , and  $m$  and  $n$  are the poloidal and toroidal mode numbers, respectively. Integrating Eq. (4) along the field line yields,

$$\tau \simeq \int_{-\zeta_{\max}}^{\zeta_{\max}} \frac{d\vartheta}{d\zeta} G(\zeta) d\zeta, \quad (5)$$

where  $\zeta_{\max}$  denotes the maximum value of  $\zeta$  in the field-line tracing and Gaussian window function  $G(\zeta) = \alpha / (\zeta_{\max} \sqrt{\pi}) \exp(-\alpha^2 \zeta^2 / \zeta_{\max}^2)$  with a numerical parameter  $\alpha$  is used to eliminate the end effect [4]. The specific volume  $U = d\psi/dV$  is also calculated using the same procedure [9]:

$$U \simeq \int_{-\zeta_{\max}}^{\zeta_{\max}} \frac{1}{B^\zeta} G(\zeta) d\zeta, \quad (6)$$

where  $\psi$  and  $V$  are the toroidal flux divided by  $2\pi$  and the volume enclosed by the magnetic surface, respectively. In deriving Eq. (6), we exploit the fact that  $U = d\psi/dV$  is equivalent to the field-line integral of  $B^\zeta$ , or  $U = \int (1/B^\zeta) d\zeta$ , see Ch.12 of [10]. Since the Todoroki's method computes the field-line integral, it can be used to evaluate the field-line average of any quantity as

$$\bar{A} = \int A \frac{dl}{B} / \int \frac{dl}{B} \simeq \frac{1}{U} \int_{-\zeta_{\max}}^{\zeta_{\max}} \frac{A}{B^\zeta} G(\zeta) d\zeta, \quad (7)$$

where  $A = A(\rho, \theta, \zeta)$  is an arbitrary function.

The field-line average  $\bar{A}$  is not necessarily a constant on a surface but depends on field lines on which the integral is performed, indicating that it cannot be used to label

surfaces as the radial coordinate  $\rho$ . In fact, this can occur on rational surfaces in non-axisymmetric devices. Practically, however,  $\bar{A}$  can be used as  $\rho$  in many typical situations where continuous nested surfaces exist. This is justified as follows. On an irrational surface,  $\bar{A}$  can be used to find the flux surface average  $\langle A \rangle = \int d\theta d\zeta \sqrt{g} A / \int d\theta d\zeta \sqrt{g}$  by following the field line long enough to cover the entire surface (refer to Ch.4.9 of [10] for more detailed discussion), where  $\sqrt{g}$  is the Jacobian of  $(\rho, \theta, \zeta)$  coordinates. Concerning the rational surface, as every rational surface can be approximated by an infinitesimally close irrational surface,  $\langle A \rangle$  on the rational surface should be continuous and infinitesimally close to those on neighboring irrational surfaces. Thus,  $\bar{A}$  on the rational surface is expected to converge to a unique value, regardless of the field lines;  $\bar{A} \rightarrow \langle A \rangle$  for every field line lying on a rational surface. This enables us to use  $\bar{A}$  as the radial coordinate by choosing  $A$  such that  $\bar{A}$  is monotonically increasing, for example,  $A = r^2$ . In this study, we use  $\rho = \sqrt{r^2}/a_0 \equiv \rho_{DM}$  for the method. Note that the discussion here is rather intuitive than rigorous. The validity of the convergence of  $\bar{A}$  toward  $\langle A \rangle$  would be sensitive to the magnitude of the nonlinear resonance on the rational surface, which could break the surface into islands/chaos. In that case, the method is not applicable because the flux surface average is not meaningful, making it inappropriate to define the surface label by the field-line average. This topic is left for future study.

The transformation between  $(r, \vartheta, \zeta)$  and  $(\rho_{DM}, \theta, \zeta)$  is numerically constructed as follows. First, as in the previous subsection, the poloidal angle  $\theta$  is chosen as  $\theta = \vartheta$ . The remaining task is to determine the transformation of  $r \Leftrightarrow \rho_{DM}$  at each  $\theta$  and  $\zeta$ , which gives the overall transformation. Figure 1 (b) shows the schematic view of the method. As shown in the figure, field lines starting from all initial points (depicted by open circles) densely covering the entire computational domain inside the LCFS are followed, which gives  $\rho_{DM}$  at each initial point,  $\rho_{DM}(r_i, \vartheta_j, \zeta_k)$  ( $i, j, k = 1, 2, 3, \dots$ ), where  $r_i = i\Delta r$ ,  $\vartheta_j = (j-1)\Delta\vartheta$ , and  $\zeta_k = (k-1)\Delta\zeta$  denotes the initial point from which the field line is traced;  $\Delta r = a/N_r$ ,  $\Delta\vartheta = 2\pi/N_\vartheta$ , and  $\Delta\zeta = (2\pi/N)/N_\zeta$ ;  $a$  is the radius of the LCFS along the  $(\vartheta_j, \zeta_k)$  line segment;  $N$  is the number of field periods; and  $N_{r, \vartheta, \zeta}$  is the number of grids in each direction. In following the field lines, we can compute  $\rho_{DM} = \sqrt{r^2}/a_0$  with the embarrassingly parallel approach due to the independence of Eq. (7) for each field line. That is,  $\rho_{DM} = \sqrt{r^2}/a_0$  of each field line can be computed entirely in parallel. Note that points with the same  $\rho_{DM}$  value belong to the identical surface. Hereafter, we refer to the method as dense mapping; we need to follow multiple field lines to identify a flux surface in this method, whereas the single long field-line tracing gives a complete information on a surface in simple mapping. After determining  $\rho_{DM}$  at every point inside the LCFS, the numerical inversion of  $\rho_{DM}(r, \vartheta, \zeta)$  into  $r(\rho_{DM}, \theta, \zeta)$  at each  $(\theta, \zeta)$  is easily calculated using numer-

ical interpolation, which results in the global transformation.

The present method relies only on the average along the field line,  $\bar{r}^2$ , to find the transformation between  $(\rho_{DM}, \theta, \zeta) \Leftrightarrow (r, \vartheta, \zeta)$ . Using the average as the radial coordinate instead of local coordinate values, the transformation between  $r \Leftrightarrow \rho_{DM}$  is expected to be smooth and continuous. This is examined in the next section.

### 3. Numerical Results

In this section, simple mapping and dense mapping are tested by applying them to a non-axisymmetric magnetic field. Here, we consider a model 3D toroidal magnetic field derived by Dommaschk [11], where the magnetic field  $\mathbf{B}$  is given by the scalar potential  $V$ , called the Dommaschk potential, as  $\mathbf{B} = \nabla V(R, \phi, Z)$ . The Dommaschk potential  $V$  is determined to satisfy the solenoidal condition of  $\mathbf{B}$ ,  $\nabla \cdot \mathbf{B} = 0$ , and is formally expressed as

$$V(R, \phi, Z) = \frac{B_0 R_0}{2\pi} \phi + \frac{B_0 R_0}{2\pi} \sum_{N,l} \left\{ V_{N,l}^{(c)}(R, Z) \cos(N\phi) + V_{N,l}^{(s)}(R, Z) \sin(N\phi) \right\}, \quad (8)$$

where  $R_0$  and  $B_0$  are given numerical constants that represent the position of the reference magnetic axis and the reference magnitude of the magnetic field, respectively;  $V_{N,l}^{(c)}$  and  $V_{N,l}^{(s)}$  denote analytic functions of  $(R, Z)$  for a given  $N$  and  $l$ ;  $N$  represents the number of field periods, and  $l$  (roughly) controls the shape of the poloidal cross-section. It can be seen that  $\nabla \times \mathbf{B} = \nabla \times \nabla V = 0$ , implying that the field is current-free. An important feature of the Dommaschk potential is that  $\nabla \cdot \mathbf{B} = 0$  is satisfied for arbitrary choices of  $N$  and  $l$ .

In this study, we use a simple Dommaschk potential  $V$  presented in [12], where the number of field periods is chosen as  $N = 5$ , and explicit expressions for  $V_{N,l}^{(c)}$  and  $V_{N,l}^{(s)}$  are described in detail. Parameters  $R_0$  and  $B_0$  are arbitrary, and results presented below do not change for any choice. It should be noted that the simple Dommaschk potential used here has a planar magnetic axis,  $R_{ax}(\phi) = R_0$ . Figure 2 shows Poincaré plots on the  $\phi = 0$  and  $(2\pi/N)/4$  planes, respectively. Here, the magnetic field-line tracing is performed using the 4th order Runge–Kutta method with  $\Delta\phi = (2\pi/N)/256$ , where the step size is determined from convergence tests. The number of toroidal turns (the number of periods that the field lines are followed) is chosen as  $N_{\text{turn}} = 1024$  to make the Poincaré plots visible, and  $\alpha = 3$  is used for the Gaussian window function  $G(\zeta)$  with  $\zeta_{\text{max}} = 64 \times (2\pi/N)$ , where  $\alpha = 3$  is a typical choice according to Ref. [9]. From the figure, the magnetic field is found to have simple elliptic surfaces. Figure 3 shows the  $|\tau|$  profile as a function of  $\rho_{PM}$ , where  $\tau$  is calculated using Eq. (5). Note that the rotational transform  $\tau$  is negative because  $B^z < 0$  ( $B^z > 0$ ) for the field considered here. From the figure, we can see that  $|\tau|$  of the field is relatively

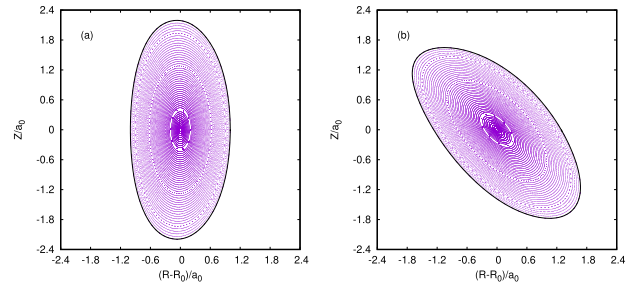


Fig. 2 Poincaré plots of magnetic field lines at (a)  $\phi = 0$  and (b)  $\phi = (2\pi/N)/4$ . A thick black line denotes the last closed flux surface.

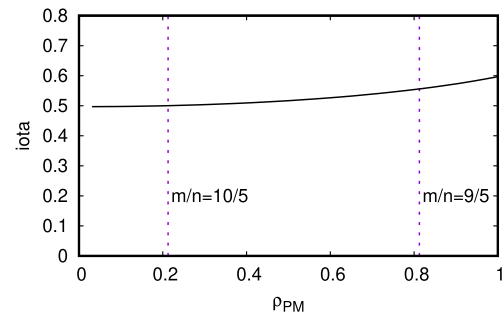


Fig. 3 Rotational transform  $|\tau|$  profile as a function of  $\rho_{PM}$ . The vertical lines in the figure denote the position of typical low-order surfaces with  $m/n = 10/5$  and  $m/n = 9/5$ , respectively.

small, with  $|\tau| \lesssim 0.5$  at the axis and  $\approx 0.6$  at the LCFS. In Fig. 3, positions of two typical low-order rational surfaces of  $m/n = 10/5$  and  $9/5$  are also shown.

In what follows, we compare the constructed surfaces and some derived quantities obtained by simple mapping and dense mapping, respectively, for the magnetic field in Fig. 2. The 4th order Runge–Kutta method is used again for the field-line tracing, where the step size  $\Delta\phi = (2\pi/N)/256$  is the same as that used in Fig. 2. The cubic splines are used for the interpolation in both methods with  $(N_r, N_\theta, N_\zeta) = (80, 256, 256)$ . For simple mapping, the number of toroidal turns is determined as  $N_{\text{turn}} = 1024$  from convergence tests. For dense mapping, we used parameters  $\alpha = 3$  and  $\zeta_{\text{max}} \equiv N_{\text{turn}} \times (2\pi/N) = 64 \times (2\pi/N)$ , as used in Fig. 3. It should be noted that the choice of  $\zeta_{\text{max}}$  ( $N_{\text{turn}}$ ) for a given  $\alpha$  is quite important for dense mapping and will be discussed later in this section.

First, we examine  $\rho_{DM} = \text{const.}$  surfaces constructed using dense mapping. Figure 4 shows the contours of  $\rho_{DM}$  surfaces on the  $\phi = 0$  and  $(2\pi/N)/4$  planes. It is confirmed in Fig. 4 that the shapes of the surfaces are similar to those in Fig. 2, which shows that the dense mapping method works well to construct surfaces. The accuracy of the constructed surfaces in Fig. 4 is quantitatively verified using the residual level of the radial component of  $\mathbf{B}$ ,

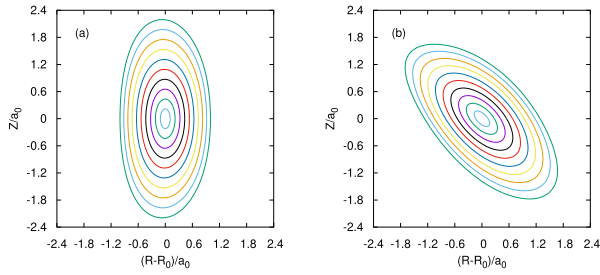


Fig. 4 Contour of  $\rho_{DM}$  at (a)  $\phi = 0$  and  $\phi = (2\pi/N)/4$  constructed by dense mapping.

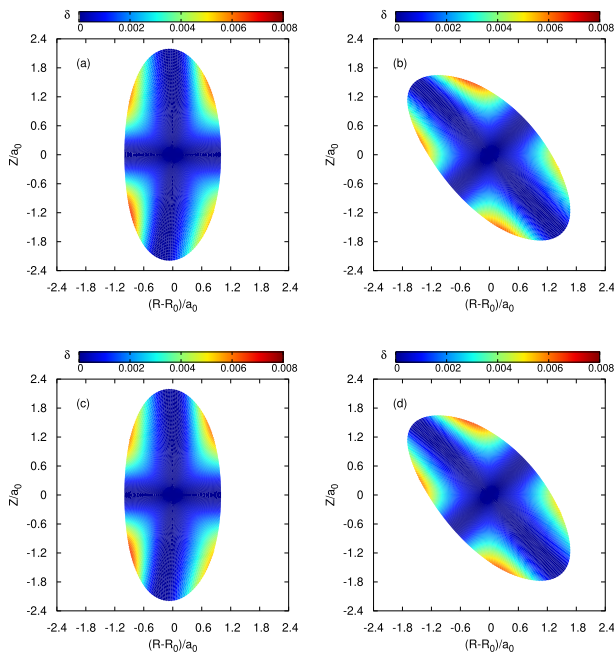


Fig. 5 Variation of the residual level  $\delta$  in Eq. (9) evaluated for the surfaces constructed by simple mapping (top) and dense mapping (bottom): (a) and (c)  $\phi = 0$  plane; (b) and (d)  $\phi = (2\pi/N)/4$  plane.

$B^\rho = \mathbf{B} \cdot \nabla \rho$ , which should be zero if constructed surfaces are actually magnetic surfaces. The residual  $\delta$  is defined as

$$\delta \equiv \left\{ B - \left( B^\theta B_\theta + B^\zeta B_\zeta \right)^{1/2} \right\} / B_0. \quad (9)$$

From the relation of  $B^2 = B^\rho B_\rho + B^\theta B_\theta + B^\zeta B_\zeta$ , it can be readily found that  $\delta$  becomes small when the magnetic field lies on the surface (the surface-normal component of  $\mathbf{B}$ ,  $B^\rho$ , becomes small), where  $B_u = (\partial \mathbf{r} / \partial u) \cdot \mathbf{B}$  ( $u = \rho, \theta, \zeta$ ) is the covariant component of  $\mathbf{B}$ . The residual  $\delta$  values evaluated for both methods are shown in Fig. 5 on the same  $\phi$  planes as in Figs. 2 and 4. It is confirmed in Fig. 5 that residuals of both methods are at the same level, which indicates that dense mapping constructs surfaces within the same accuracy as simple mapping.

Next, the radial derivative  $\partial r / \partial \rho$  is examined, where  $\rho = \rho_{PM}$  and  $\rho = \rho_{DM}$  are used for simple mapping and

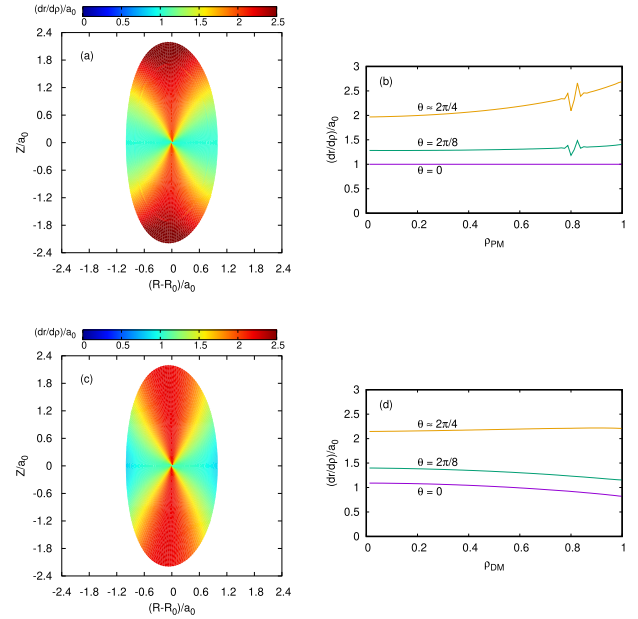


Fig. 6 Radial derivative of  $r = r(\rho, \theta, \zeta)$ ,  $\partial r / \partial \rho$ , for the surfaces constructed by simple mapping (top,  $\rho = \rho_{PM}$ ) and dense mapping (bottom,  $\rho = \rho_{DM}$ ): (a) and (c) contour of  $\partial r / \partial \rho$  on the  $\phi = 0$  plane; (b) and (d)  $\partial r / \partial \rho$  profile as a function of the corresponding radial coordinate  $\rho$  for several  $\theta$  values on the  $\phi = 0$  plane.

dense mapping, respectively. Figures 6(a) and (c) show contour plots of  $\partial r / \partial \rho$  on the  $\phi = 0$  plane for respective methods, and (b) and (d) show the corresponding  $\partial r / \partial \rho$  profile as a function of  $\rho$  at several  $\theta$  values indicated in the figures. From Figs. 6(a) and (b), the discontinuity in  $\partial r / \partial \rho$  occurs near the edge region of  $\rho_{PM} \simeq 0.8$  for simple mapping, where the low-order rational surface of  $m/n = 9/5$  is located, whereas the discontinuity disappears for dense mapping, as shown in the bottom figures in Fig. 6.

To see how dense mapping improves  $\partial r / \partial \rho$ ,  $r$  profiles of both methods are compared in Fig. 7, where  $r$  is plotted as a function of  $\rho_{PM}$  for several  $\theta$  values on the  $\phi = 0$  plane to make a detailed comparison of both methods. This figure confirms that  $r$  for both methods shows a fairly good agreement, except in neighborhoods of the  $m/n = 9/5$  surface at  $\rho \simeq 0.8$ . It can be seen in the figure that  $r = r(\rho_{PM})$  of simple mapping locally shows a somewhat flattened profile, while the radius  $r$  constructed by dense mapping is slightly modified near the rational surface (see the enlarged view at the bottom of Fig. 7). Although the change in  $r$  is quite small, it makes  $\partial r / \partial \rho$  of dense mapping smooth, indicating that the field-line average in constructing the radial coordinate  $\rho$  introduces a smoothing effect on the transformation between  $\rho$  and  $r$ . The smoothing effect depends on  $\zeta_{max}$ , or  $N_{turn}$  used in computing the field-line average. For example, for the configuration considered here,  $r = r(\rho)$  of dense mapping also tends to show similar flattening as simple mapping for a larger  $N_{turn} \gtrsim 100$ , resulting in the discontinuity, although the discontinuous behavior in dense

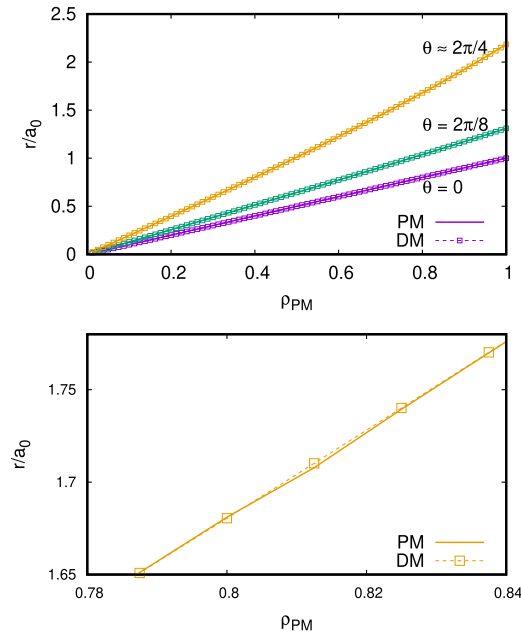


Fig. 7 (Top) Constructed radius  $r = r(\rho, \theta, \zeta)$  as a function of  $\rho_{PM}$  by simple mapping (solid lines denoted by PM) and dense mapping (symbols by DM) for several  $\theta$  values on the  $\phi = 0$  plane. (Bottom) Enlarged view for the  $\theta \approx 2\pi/4$  case at  $0.78 \lesssim \rho_{PM} \lesssim 0.84$ .

mapping is not so significant compared to that observed in simple mapping. From numerical tests,  $N_{\text{turn}} = 64$  with  $\alpha = 3$  has been used here. Unfortunately, however, it is difficult to know an optimal choice of  $N_{\text{turn}}$  and  $\alpha$  for general cases; since they could generally depend on configurations, the parameters should be chosen carefully. In contrast, adequately large  $N_{\text{turn}}$  ( $N_{\text{turn}} \gtrsim 1000$  for the case here) should be used in simple mapping. Since  $N_{\text{turn}}$  corresponds to the number of points in Poincaré map in this method, the poloidal interpolation to obtain a surface in simple mapping would not work well when  $N_{\text{turn}}$  is small.

Identifying the cause of the discontinuity is difficult. As shown in Fig. 5, the accuracy of the constructed surfaces is almost the same for both methods, implying that the discontinuity occurs physically rather than numerically. A possible candidate for the discontinuity is the nonlinear resonance near the low-order rational surface, which can break the surfaces and lead to the formation of islands and/or chaotic regions. Although the rational surface of  $m/n = 9/5$ , where the discontinuity appears, is not actually broken, the resonance could deteriorate the surface through the integrability breaking at that point. Furthermore, every low-order rational surface does not necessarily yield a discontinuous radial derivative. In fact, as found in  $\rho \approx 0.2$  of simple mapping in Fig. 6, the  $m/n = 10/5$  rational surface does not exhibit the discontinuity. Responding to these questions is beyond the scope of this work and is left for future studies.

Finally, the derivatives of  $r$  in the  $\theta$  and  $\zeta$  directions

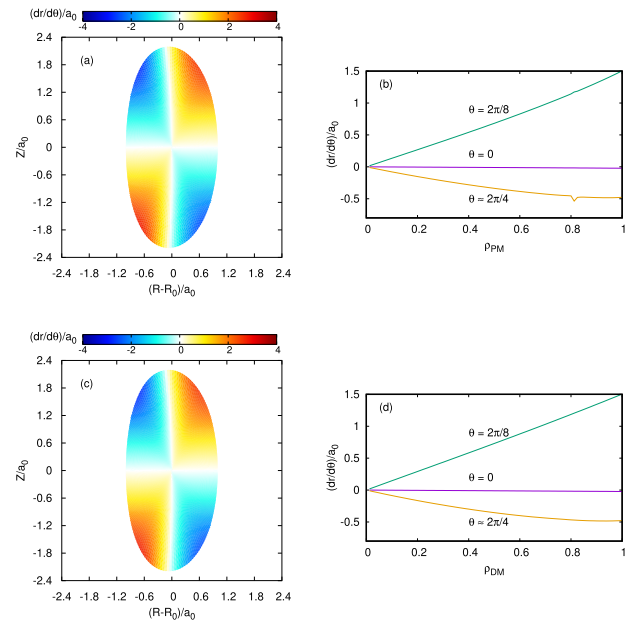


Fig. 8 Poloidal angle derivative of  $r = r(\rho, \theta, \zeta)$  for the surfaces constructed by simple mapping (top,  $\rho = \rho_{PM}$ ) and dense mapping (bottom,  $\rho = \rho_{DM}$ ): (a) and (c) contour of  $\partial r / \partial \theta$  on the  $\phi = 0$  plane; (b) and (d)  $\partial r / \partial \theta$  profile as a function of the corresponding radial coordinate  $\rho$  for several  $\theta$  values on the  $\phi = 0$  plane.

are examined. Figures 8 (a) and (c) show contour plots of  $\partial r / \partial \theta$  on the  $\phi = 0$  plane for simple mapping and dense mapping, respectively; (b) and (d) show the corresponding  $\partial r / \partial \theta$  profiles as a function of  $\rho$  for several  $\theta$  values indicated in the figures, where  $\rho = \rho_{PM}$  and  $\rho = \rho_{DM}$  are used in (b) and (d), respectively. From Fig. 8 (b),  $\partial r / \partial \theta$  shows a similar discontinuity as in Fig. 6 (b), although it is not so significant compared with that in  $\partial r / \partial \rho$  (in fact, the discontinuity disappears for the  $\theta = 2\pi/8$  case, where the clear discontinuity occurs for  $\partial r / \partial \rho$ ). The discontinuity can be successfully avoided again by dense mapping, as shown in Fig. 8 (d). The situation is similar to that of the  $\zeta$ -derivative. This indicates that the smoothing effect by dense mapping can also improve the continuity in the derivatives along the surface.

## 4. Summary

In this study, we proposed a novel numerical method for constructing continuous and smooth flux surfaces for general 3D magnetic configurations with good nested surfaces. The method is called dense mapping. In this method, multiple field lines starting from all grid points in the computational domain are simultaneously traced to compute the field-line average at each point. The field-line average obtained for all grid points through this process was then used to define the label of the flux surface, or the radial coordinate  $\rho$  in the magnetic coordinates. A model 3D toroidal magnetic field of Dommaschk type was used

to examine the continuity of surfaces constructed using two methods: dense mapping and the conventional method based on the Poincaré map (simple mapping). It was found that simple mapping induces various numerical discontinuity in the derivatives of  $r$  near a low-order rational surface. Conversely, it was demonstrated that the discontinuity can be successfully avoided by dense mapping owing to the smoothing effect on the transformation between  $\rho$  and  $r$ . It should be noted that surfaces of dense mapping around the low-order rational surface are not exactly the same as those of the Poincaré map; the smoothing effect slightly changes the surfaces within a reasonable accuracy. Although it is not mathematically rigorous, the proposed method has a general applicability to any 3D magnetic field as long as continuous nested surfaces are seen to exist, as it only relies on the field-line average.

The computational cost of dense mapping is much higher than that of the conventional mapping. This is because the former method requires one to follow all field lines starting from all grid points in the domain to identify positions of surfaces globally, whereas the single field-line tracing gives a transformation on a surface in the latter. However, in practice, because multiple field-line tracings in dense mapping can be performed independently for each field line, we can reduce the computational time on recent computers with many cores/nodes by exploiting embarrassingly parallel computations of multiple field-line tracings.

It should be emphasized that the construction of the smooth magnetic coordinates is crucial for subsequent calculations such as stability analyses and transport simulations. Because low-order rational surfaces usually exist in 3D toroidal magnetic fields, e.g. 3D MHD equilibria by HINT [13] and magnetic fields determined by the Biot–Savart law in coil optimizations [14], the discontinuity around the rational surfaces could be problematic in

such equilibria. The dense mapping method presented here provides a simple and practical tool to construct smooth magnetic coordinates for the equilibria, which are used as input for the subsequent calculations.

## Acknowledgments

The author would like to thank Drs. M. Nakata, Y. Suzuki and H. Sugama in NIFS and Dr. Y. Idomura in JAEA for their useful comments on this work. The author is indebted to an anonymous reviewer for providing him helpful comments and questions to improve the manuscript. The computations in this work were performed on JFRS-1 at IFERC-CSC and Plasma Simulator at NIFS. This work was supported by JSPS KAKENHI Grant No. JP19K03801 and the NIFS Collaborative Research Program NIFS16KNST103.

- [1] A.H. Boozer, *Phys. Fluids* **25**, 520 (1982).
- [2] G. Kuo-Petravic *et al.*, *J. Comput. Phys.* **51**, 261 (1983).
- [3] G. Kuo-Petravic and A.H. Boozer, *J. Comput. Phys.* **73**, 107 (1987).
- [4] A.H. Reiman and H.S. Greenside, *J. Comput. Phys.* **75**, 423 (1988).
- [5] V.V. Nemov, *Nucl. Fusion* **28**, 1727 (1988).
- [6] X. Bonnin *et al.*, *Nucl. Fusion* **45**, 22 (2005).
- [7] S.A. Bozhenkov *et al.*, *Fusion Eng. Des.* **88**, 2997 (2013).
- [8] I. Predebon *et al.*, *Plasma Phys. Control. Fusion* **60**, 045003 (2018).
- [9] J. Todoroki, *J. Plasma Fusion Res.* **79**, 321 (2003).
- [10] W.D. D’haeseleer, W.N.G. Hitchon, J.D. Callen and J.L. Shohet, *Flux Coordinates and Magnetic Field Structure* (Springer Berlin Heidelberg, Berlin, Heidelberg, 1991).
- [11] W. Dommaschk, *Comput. Phys. Commun.* **40**, 203 (1986).
- [12] P. Merkel, *J. Comput. Phys.* **66**, 83 (1986).
- [13] Y. Suzuki *et al.*, *Nucl. Fusion* **46**, L19 (2006).
- [14] C. Zhu *et al.*, *Nucl. Fusion* **58**, 016008 (2018); *ibid.* **60**, 089601 (2020).